

Ultra-sensitive atom imaging for matter-wave optics

This article has been downloaded from IOPscience. Please scroll down to see the full text article.

2011 New J. Phys. 13 115012

(<http://iopscience.iop.org/1367-2630/13/11/115012>)

View [the table of contents for this issue](#), or go to the [journal homepage](#) for more

Download details:

IP Address: 27.33.54.131

The article was downloaded on 06/01/2012 at 04:16

Please note that [terms and conditions apply](#).

Ultra-sensitive atom imaging for matter-wave optics

**M Pappa^{1,2}, P C Condylis^{1,3}, G O Konstantinidis^{1,2}, V Bolpasi^{1,2},
A Lazoudis¹, O Morizot^{1,4}, D Sahagun^{1,3}, M Baker^{1,5}
and W von Klitzing^{1,6}**

¹ IESL-FORTH, Vassilika Vouton PO Box 1527, GR-71110 Heraklion, Greece

² Physics Department, University of Crete, GR711 03 Heraklion Crete, Greece

³ Centre for Quantum Technologies, National University of Singapore,

3 Science Drive 2, 117542 Singapore, Singapore

E-mail: darkimaging@bec.gr

New Journal of Physics **13** (2011) 115012 (20pp)

Received 31 May 2011

Published 28 November 2011

Online at <http://www.njp.org/>

doi:10.1088/1367-2630/13/11/115012

Abstract. Quantum degenerate Fermi gases and Bose–Einstein condensates give access to a vast new class of quantum states. The resulting multi-particle correlations place extreme demands on the detection schemes. Here we introduce diffractive dark-ground imaging as a novel ultra-sensitive imaging technique. Using only moderate detection optics, we image clouds of less than 30 atoms with near-atom shot-noise-limited signal-to-noise ratio and show Stern–Gerlach separated spinor condensates with a minority component of only seven atoms. This presents an improvement of more than one order of magnitude when compared to our standard absorption imaging. We also examine the optimal conditions for absorption imaging, including saturation and fluorescence contributions. Finally, we discuss potentially serious imaging errors of small atom clouds whose size is near the resolution of the optics.

⁴ Current address: Université de Provence, Physique des Interactions Ioniques et Moléculaires (UMR 6633), Centre de St Jérôme, Case C21, F-13397 Marseille Cedex 20, France.

⁵ Current address: The University of Queensland, Brisbane St Lucia, QLD 4072, Australia.

⁶ Author to whom any correspondence should be addressed.

Contents

1. Introduction	2
2. Absorption	3
3. Absorption imaging	3
3.1. Signal in absorption imaging	3
3.2. Noise in absorption imaging	6
4. Fluorescence imaging	6
5. Dark-ground imaging	8
5.1. Noise in dark-ground imaging	9
5.2. Technical noise in dark-ground imaging	10
5.3. Experimental dark-ground imaging	10
6. Imaging errors	11
7. Optimal conditions for the imaging of small atom number clouds	14
7.1. Optimal detuning and saturation	14
7.2. Optimal exposure time	15
7.3. Optimal size of the dark spot and probe beam	16
7.4. Optimal cloud size	16
7.5. Minimum detectable atom number	17
8. Conclusions	17
Acknowledgments	17
Appendix A. Experimental setup	17
Appendix B. Additional graphs	20
References	20

1. Introduction

In recent years atomic physics has made enormous progress in its ability to manipulate and coherently control atoms. Since the first Bose–Einstein condensation (BEC) of dilute gases in 1995 [1–3], ultra-cold atom samples have become an almost universal resource. Early experiments studied BEC physics deep into the Thomas–Fermi regime using a rather large number of atoms. More recently, the focus has shifted toward correlations, squeezing and entanglement of small atomic samples in one, two or three dimensions [4–6]. In matter-wave interferometers, atom number squeezing combined with atom shot-noise-limited imaging would make Heisenberg-limited detection possible, where sensitivity scales with atom number rather than its square root [7]. In order to probe these strongly correlated quantum states, it is essential to use highly accurate and sensitive imaging methods [8].

The ultimate detector would be capable of imaging matter waves with single-atom resolution *in situ*. Trapped atoms are readily detected using fluorescence techniques, as has been demonstrated for magneto-optic traps [9], single dipole traps [10] and, more recently, optical lattices [11, 12]. In these cases, the detected signal is dominated by trapping potential in the presence of detection light, rather than the initial shape of the matter wave. In some cases, it is already possible to image free single atoms, albeit some distance below the atom trap. Examples include multi-channel plate detection of metastable helium [13] and fluorescence imaging with

a light sheet [14]. In many cases, it would be desirable to image the atoms *in situ*, for example in order to study the expansion of a BEC. To this end, a variety of imaging techniques have successfully been demonstrated for large atomic samples. These include standard destructive absorption [15], non-destructive dispersive dark-ground [16], pure phase-contrast [17], diffraction-contrast [18] and spatial heterodyne imaging [19]. A conclusive comparison of minimally destructive imaging techniques shows that they are largely equivalent [20]. *In situ* imaging of very small atomic samples still remains an important challenge.

In this paper, we present resonant diffractive dark-ground imaging as a novel technique to image extremely small atom numbers. Using dark-ground imaging, we can picture atom clouds down to only 30 atoms using very moderate detection optics. We begin in section 2 with a concise description of the absorption of light by an atom cloud including saturation. In section 3 we look at the standard absorption imaging, and use this in section 3.1 to derive an analytic expression for the atom column density in absorption imaging fully taking into account the contribution of fluorescence and saturation effects. This is followed by a brief discussion of noise in section 3.2. We present a brief discussion of fluorescence imaging in section 4 and turn to diffractive dark-ground imaging in section 5. We demonstrate an improvement of the picture quality by about an order of magnitude allowing us to detect atom clouds containing only a few tens of atoms. In section 6 we discuss imaging errors, which can reduce the atom numbers detected and lead to deformations of the apparent shape of an atom cloud. We conclude with a discussion in section 7 of the optimal imaging conditions for both absorption and dark-ground imaging.

2. Absorption

As the probe beam propagates through the atom cloud along z , its intensity decays as $\frac{dI}{dz} = -n_3(z)\sigma(z)I$, where n_3 is the density of atoms and $\sigma(z) = \sigma_0/[1 + s(z) + \delta^2]$ is the cross-section containing the saturation parameter $s(z)$, which becomes smaller as light travels across the cloud. σ_0 stands for the resonant cross-section at very low saturation parameters, which contains corrections due to the structure of the excited state, and the different Zeeman sublevel populations [21]. We define I_0 and I_T as the initial and transmitted intensity, respectively, $s_0 = I_0/I_{\text{sat}}$ as the initial resonant saturation parameter and $\sigma = \sigma_0/(1 + s_0 + \delta^2)$ as the initial cross-section. Neglecting contributions from the fluorescence, we find the transmittance ($T = I_T/I_0$) of a column density n as

$$T = \frac{1 + \delta^2}{s_0} W \left[\frac{s_0}{1 + \delta^2} \exp \left(\frac{s_0 - n\sigma_0}{1 + \delta^2} \right) \right], \quad (1)$$

where W is the Lambert function of the first kind and $\delta = f/\Delta f$ is the normalized detuning with the half-width at half-maximum (HWHM) linewidth Δf of the imaging transition at $s_0 \ll 1$. For small saturation parameters ($s_0 \ll 1$) and/or low optical depths ($n\sigma$), (1) is equivalent to the well-known Beer–Lambert law: $n = -\ln(T)/\sigma$.

3. Absorption imaging

3.1. Signal in absorption imaging

The most common imaging technique in matter-wave optics is absorption imaging, where a probe beam is shone onto the atomic cloud and then imaged onto a camera. As can be seen in

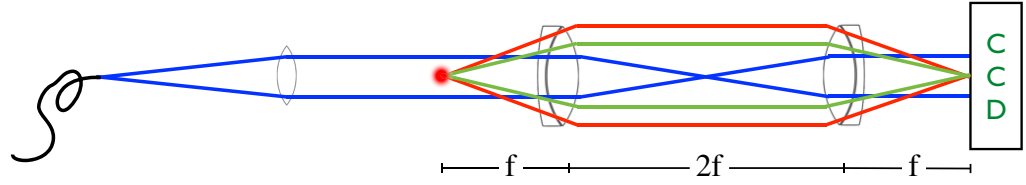


Figure 1. A typical optical setup for absorption optics using a relay telescope in the $4f$ configuration. Left to right, the probe beam (blue) is launched from a single-mode optical fiber (black) and collimated by a first lens, after which it interacts with the atomic cloud. Two sets of lenses relay the diffracted image of the absorption (green), the fluorescence (red) and the probe beam (blue) to a charge coupled device (CCD) camera. Here the absorption and probe beams interfere to form, together with the fluorescence, the image of the absorption. Often an additional microscope objective is used to magnify the image.

figure 1, the image on the camera has three components: the probe beam (blue), the diffracted and refocused absorption (green), and the fluorescence (red). The probe beam and the absorption are coherent with each other but incoherent with the fluorescence. Equation (1) describes the loss of light in the probe beam, where the atom cloud forms a dip on a bright background.

A small fraction (Ω) of the fluorescence from the atoms is emitted into the solid angle of the detection optics, where it reduces the absorption dip. On its way to the camera, a fluorescence photon travels through a cone-shaped section of the atom cloud, where it might be absorbed. We can neglect the radial distribution of the atom density in the cloud if the opening of the detection cone over the length Δz of the cloud is small compared to the smallest transverse size $\Delta \rho$ of the cloud. For a given numerical aperture (NA) of the detection optics, this condition is fulfilled if $\Delta \rho \gg \text{NA} \Delta z$. In this case we can take into account the contribution of the fluorescence in the differential equation as $\frac{dI}{dz} = -n_3(1 - \Omega)\sigma(z)I$. This modified differential equation takes into account the reduction of the absorption dip at the camera due to the fluorescence including its reduction by reabsorption as it travels across the atom cloud. If the optical depths ($\sigma n \ll 1$) are small, this equation holds true for any cloud shape. The relative intensity of the absorption image at the camera ($T_{\text{abs}} = I_{\text{T}}/I_0$) is

$$T_{\text{abs}} = \frac{1 + \delta^2}{s_0} W \left[\frac{s_0}{1 + \delta^2} \exp\left(\frac{s_0 - n(1 - \Omega)\sigma_0}{1 + \delta^2}\right) \right]. \quad (2)$$

The magenta-colored line in figure 2 shows the signal strength of the absorption image $I_0(1 - T_{\text{abs}})$ as a function of the optical depth for our typical experimental conditions.

In a typical experiment, usually three pictures are taken: an absorption image, a reference image, and a background image. For the absorption image, one shines the probe beam onto the atoms and then images it onto the camera (I_{abs}). The reference image contains only the probe beam (I_{ref}). The background image (I_{bgr}) is taken without the probe beam or atoms. We can then calculate, for each pixel, $T_{\text{abs}} = (I_{\text{abs}} - I_{\text{bgr}})/(I_{\text{ref}} - I_{\text{bgr}})$ and $s_0 = (I_{\text{ref}} - I_{\text{bgr}})/I_{\text{sat}}$.⁷ We can

⁷ If the probe beam contains a small but non-negligible fraction (α) of non-resonant light—such as the repumper or a non-resonant background—then $T_{\text{abs}} = (I_{\text{abs}} - I_{\text{bgr}} - \alpha I_{\text{ref}})/[(1 - \alpha)I_{\text{ref}} - I_{\text{bgr}}]$ and $s_0 = [(1 - \alpha)I_{\text{ref}} - I_{\text{bgr}}]/I_{\text{sat}}$. Note also that the quantum efficiency of the camera and the transmission of the detection optics need to be taken into account for the saturation intensity.

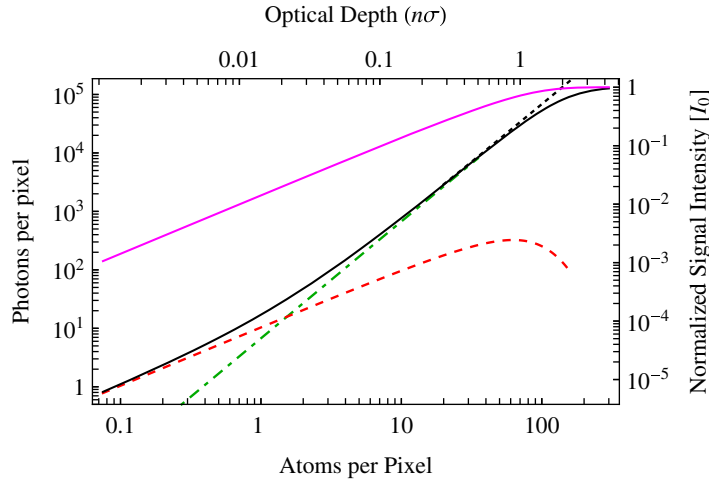


Figure 2. Signal strength in imaging: a plot of the signal intensity of absorption, fluorescence and dark-ground images versus atom column densities. The left and lower axes stand for the number of photons and atoms per pixel, respectively, using the experimental parameters described below. The upper axis is the optical depth in units of $n\sigma$, and the right axis is the image intensity relative to the intensity of the probe beam, here $I_0 = I_{\text{sat}}$. Rhodamine — signal in absorption imaging $[I_0(1 - T)]$ using (2). Black — full dark-ground signal according to (7). Red - - - approximation of the dark-ground signal for low absorbances ($n\sigma \ll 1$) according to (8). - - - contribution of the fluorescence to the dark-ground and absorption signals. Lime green —·— contribution to the dark-ground signal by light, which was diffracted by the atom cloud. The parameters chosen correspond to those of figures 6(a) and (b), which used π -polarized light on the D_2 transition of ^{87}Rb with an effective pixel area of $a = 6.8 \mu\text{m}^2$ and an exposure time of $\tau = 200 \mu\text{s}$. We set $\delta = 0$, $s_0 = 1$ and $\text{NA} = 0.15$ and thus $\Omega = 0.005$. The effective pixel size was $2.6 \mu\text{m}$. Furthermore, we assume that the cloud is well resolved by the imaging optics and that its shape obeys $\Delta\rho \gg \text{NA} \Delta z$.

use (2) to calculate the column density if the size of the cloud is larger than the diffraction limit of the resolution of the imaging optics:

$$n = \frac{1 + \delta^2}{(1 - \Omega)\sigma_0} \left[-\ln(T_{\text{abs}}) + \frac{s_0}{1 + \delta^2}(1 - T_{\text{abs}}) \right]. \quad (3)$$

This equation includes the saturation caused by the probe beam and its reduction along the path through the cloud, as well as the imaged fluorescence including its reabsorption by the atoms as it travels toward the camera. For weak absorbance ($A \equiv 1 - T_{\text{abs}} \ll 1$) and/or low saturation ($s_0 \ll 1$) equation (3) turns into a modified Beer–Lambert law: $n = -\ln(T)/\sigma'$, with the effective absorption cross-section $\sigma' = (1 - \Omega)\sigma_0/(1 + s_0 + \delta^2)$. For $A \ll 1$, the column density is linear in the absorbance: $n = A/\sigma'$.

Note that even at modest absorbances and saturations this approximation slightly overestimates the column densities, thus distorting the shape of the imaged atom cloud. Even for a saturation as low as $s_0 = 0.1$ and a transmission of $T = 0.1$, using $n = -\ln(T)/\sigma'$ instead of (3) results in an error of +6%.

3.2. Noise in absorption imaging

3.2.1. Photon shot-noise. Due to the Poissonian statistics of photons in the coherent probe beam, a pixel on the camera detecting on average N photons has a photon shot-noise of $N_{\text{noise}} = \sqrt{N}$. As stated earlier, three pictures are taken: an absorption image, a reference image and a background image. The noise due to the background image can normally be neglected. Using (3) and its derivatives with respect to the photon number in the absorption and reference images times the square root of photon number itself, one finds for the photon shot-noise limit

$$\text{SNR}_{\text{abs}} = \sqrt{N_0} \left(\frac{T_{\text{abs}}[s_0(1 - T_{\text{abs}}) - \ln(T_{\text{abs}})]^2}{1 + T_{\text{abs}}[1 + s_0(4 + s_0 + s_0 T_{\text{abs}})]} \right)^{1/2} \quad (4a)$$

$$= \begin{cases} \sqrt{N_0/2} [A + (A/2)^2], & \text{for } A \ll 1, \\ \sqrt{N_0 T_{\text{abs}}} [s_0 - \ln(T_{\text{abs}})], & \text{for } T_{\text{abs}} \ll 1, \end{cases} \quad (4b)$$

where N_0 is the number of photo-electrons per pixel detected in the reference image. We neglect the contribution of camera noise. Note that using numerical methods to model the reference image [22] can largely remove the contribution of the reference image to the photon shot-noise of individual pixels. This improves the SNR_{abs} for $A \ll 1$ by a factor of $\sqrt{2}$.

In figure 3, the magenta-colored lines show the photon shot-noise-limited signal-to-noise ratio (SNR) as a function of optical depth for our typical experimental parameters. The solid line represents the full expression (4a), whereas the dashed lines show the approximate expressions of (4b). Figure B.1 shows the same plot for a much increased numerical aperture ($\text{NA} = 0.59$ and $\Omega = 0.09$) as used in [4]. Clearly, the NA of the objective has very little influence on the SNR in absorption imaging. The main effect of the increased resolution is that smaller cloud sizes can be resolved, which at a given minimal optical density contain fewer atoms.

3.2.2. Technical noise. In most experiments the detection is limited by fringes caused by small reflections from optical elements in the beam path. A reflection resulting in an intensity of $10^{-5}I_0$ at the camera would already cause fringe noise equivalent to the photon shot-noise caused by an average 25×10^3 photons. Clearly, it is very difficult to reach the photon shot-noise-limited regime. Great care has to be taken to avoid unnecessary optical surfaces and scatterers, and to use good antireflection coatings where possible. However, much of the fringe problem can be alleviated by using numerical methods to model and partially remove the interference fringes [22].

Another potential source of noise is the camera itself. Conversion and amplification noise, dark-counts and quantum efficiency all contribute to the overall SNR. A detailed description would exceed the scope of this paper. Absorption imaging does not pose very stringent requirements on the camera since in most cases the SNR is limited by photon shot-noise due to the large number of photons per pixel.

4. Fluorescence imaging

In fluorescence imaging, an atomic cloud is illuminated by a probe beam and the emitted fluorescence is imaged onto a camera using a relay telescope (figure 4). Since the collection efficiency (Ω) is proportional to the square of the numerical aperture, it is important to place a

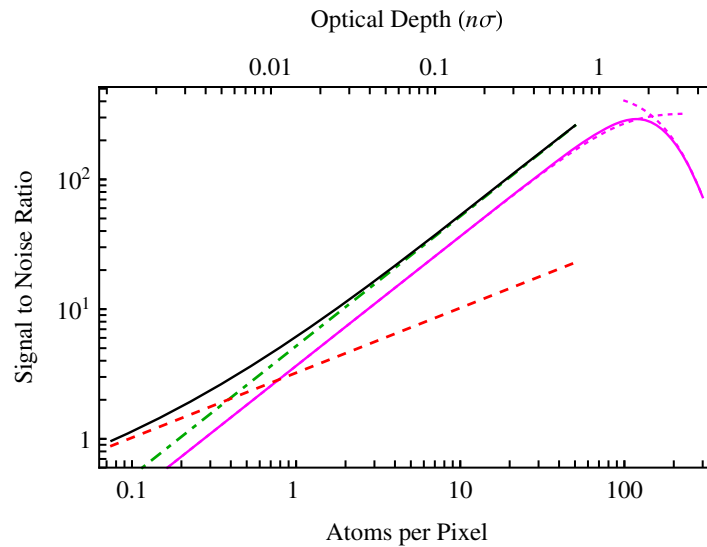


Figure 3. Photon shot-noise limited SNR: a plot of the photon shot-noise-limited SNR versus the optical depth for dark-ground, fluorescence and absorption imaging of an atom cloud. The lower axis represents the number of atoms per pixel and the upper axis the optical depth in units of $n\sigma$. Rhodamine — SNR of absorption imaging according to (4a). ······ Approximations of the SNR of absorption imaging for $n\sigma \ll 1$ and $T \ll 1$, respectively, according to (4b). Black — SNR of dark imaging for low absorbances according to (10). Red ---- SNR of the fluorescence alone. Lime green — · — SNR of the light that was diffracted by the atom cloud. The parameters are the same as those of figure 2.

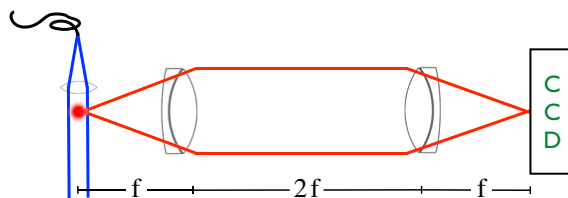


Figure 4. A typical setup for fluorescence imaging. Left to right, the probe beam (blue) is launched from a single-mode optical fiber (black) and collimated by a first lens, after which it interacts with the atomic cloud. Two sets of lenses then image the fluorescence (red) onto a CCD camera.

large lens close to the atoms. For low optical depths ($n\sigma \ll 1$), the total photon flux at the camera is proportional to the atom number. At higher optical depth, the reabsorption of the fluorescence and the attenuation of the probe beam have to be taken into account. In order to avoid a variation of the saturation parameter across the image, we will assume that the probe beam is collinear with the imaging axis. The only difference between the absorption signal (T_{abs}) in (2) and the coherent transmittance (T) in (1) is that in T_{abs} the fluorescence at the camera has been taken into account, which therefore can be calculated as the difference between the absorption signal

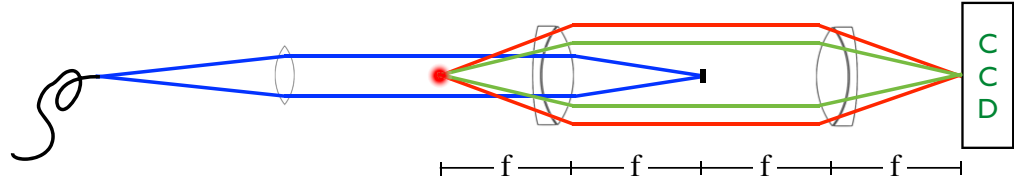


Figure 5. A typical optical setup for Fourier imaging using a relay telescope in the 4f configuration. The probe beam (blue) is launched from a single-mode optical fiber (black) and then collimated, after which it interacts with the atomic cloud. A first set of lenses collimates the fluorescence (red) and the diffracted image of the absorption (green). The same lens focuses the probe beam (blue) to a spot, at which point it is (partially) blocked by an opaque disc. A second set of lenses then images the fluorescence and diffracted probe light, where the latter interferes with the non-diffracted probe light that was transmitted through the opaque disc to form the image on the CCD camera. Often an additional microscope objective (not shown) is used to magnify the image.

(T_{abs}) and the coherent transmittance (T):

$$I_{\text{fluo}} = I_0(T_{\text{abs}} - T). \quad (5)$$

For small absorbances this reduces to $I_{\text{fluo}} = \Omega n \sigma I_0$. In this regime, the SNR is $\text{SNR}_{\text{fluo}} = \sqrt{N_0 \Omega n \sigma}$. The dashed red lines in figures 2 and 3 show the intensity of the fluorescence image and its SNR as a function of the optical depth for our typical experimental parameters. Note that at higher optical depths the signal drops due to the reabsorption of the fluorescence combined with a reduction in the saturation parameter. The fluorescence signal is usually small compared to the absorption signal. However, in dark-ground imaging at very low optical depths, the fluorescence signal can become dominant (see figure 2).

5. Dark-ground imaging

In section 3.2.1, we have seen that the SNR in absorption imaging is determined by the photon shot-noise of the probe beam. Using optical Fourier filtering, the noise contribution of the probe beam can be greatly reduced, albeit at the cost of also reducing the signal itself.

By placing a small opaque disc into the center of the Fourier plane of the image (see figure 5), the probe beam can be reduced in intensity or even blocked completely. In order to calculate the resulting image, one has to sum coherently the partially blocked light and the diffraction of the absorption and then add incoherently the fluorescence.

Let us consider as a probe beam a plane wave of initial intensity I_0 , which reduces to $I_{\text{tr}} = T I_0$ after interaction with the small atom cloud. In order to study its propagation, we have to consider its electric field amplitudes. Just after the atoms, the probing wave can be thought of as having two components: the plane wave of the probe beam (E_0) plus the localized wave of the absorption (E_{abs}) that is 180° out of phase with respect to the probe beam. The field amplitude of the probe beam is $E_0 = \sqrt{2\mu_0 c I_0}$ and that of the absorption is

$$E_{\text{abs}} = (1 - \sqrt{T}) E_0. \quad (6)$$

After the first lens—in the Fourier plane of the image—the plane wave of the probe beam focuses to a small spot, whereas the absorption is spread out. If the opaque disc is much larger than the focused probe beam though much smaller than the diffraction from the atoms, then it leaves the absorption untouched and selectively removes the intensity of the probe beam. In the image plane, the image of the atom cloud appears bright on a dark background. Assuming that transmission through the opaque disc is negligibly small, the image intensity in dark-ground imaging can be written as

$$I_{\text{dark}} = I_0[(1 - \sqrt{T})^2 + (T_{\text{abs}} - T)], \quad (7)$$

where the $(1 - \sqrt{T})^2$ term originates from the diffraction signal and the $(T_{\text{abs}} - T)$ term from the contribution from the fluorescence. With (1) we can then calculate the intensity of the full dark-ground signal, including the contribution from the fluorescence and the spatially varying saturation parameter. The result is shown as the solid black line in figure 2 using our typical experimental parameters. The dashed green line contains the pure dark-ground signal without the contribution from fluorescence and the dashed red one the fluorescence only.

In principle, (7) allows us to determine the column density of atoms from the dark-ground image. However, in order to derive an analytic expression for the atom column density, we have to assume that the optical depth is relatively low ($n\sigma_0 < s$). The intensity of the image is

$$I_{\text{dark}} = I_0 \left[\left(\frac{1}{2} n\sigma \right)^2 + \Omega n\sigma \right]. \quad (8)$$

For intermediate optical depths [$(1 + s_0 + \delta^2) > n\sigma_0 \gg 4\Omega$], the signal is dominated by the term stemming from diffraction of light by the atoms: $I_{\text{dark}} = I_0(n\sigma)^2$. For very low optical depths ($n\sigma \ll 4\Omega$), the fluorescence term dominates: $I_{\text{dark}} = I_0 n\sigma$. Figure 2 shows the full expression (7) as a solid black line and the approximation (8) as a dashed black line.

The atom column density from a dark-ground image at low optical depth ($n\sigma < 1$), including fluorescence and dark-ground contributions, is

$$n = \frac{2}{\sigma} \left(\sqrt{\frac{I_{\text{dark}}}{I_0} + \Omega^2} - \Omega \right). \quad (9)$$

Note that one requires knowledge of neither the quantum efficiency of the camera nor the transmission of the optics in order to calculate the atomic column density in dark-ground imaging.

5.1. Noise in dark-ground imaging

The signal from absorption imaging as seen in figure 2 is clearly much larger than that from dark-ground imaging. Absorption imaging, however, has large shot-noise due to the bright background of the image, which dark-ground imaging strives to eliminate. The photon shot-noise-limited SNR at low optical depth ($n\sigma \ll 1$) can be approximated as

$$\text{SNR}_{\text{dark}} = \sqrt{N_0} \sqrt{(n\sigma)^2 + \Omega n\sigma}. \quad (10)$$

This equation is shown for our standard experimental parameters as the solid black line in figure 3, which depicts the contribution from the fluorescence term ($\Omega n\sigma$) as a dashed red line and the one from the diffracted light $(n\sigma)^2$ as a dashed green line. For moderately low optical

depths ($\Omega \ll n\sigma \ll 1$), the diffraction term dominates. For very low optical depths ($n\sigma \ll \Omega$), the signal originates mainly from the fluorescence term.

Figure B.1 shows the same plot as figure 3 for a much increased numerical aperture (NA = 0.59 and $\Omega = 0.09$) as used for example in [4]. For a given optical density, the objective with larger NA collects a larger fraction of fluorescence, resulting in a higher SNR, especially at low optical densities. Furthermore, the higher resolution means that smaller cloud sizes can be resolved, which at a given minimal optical density contain fewer atoms.

5.2. Technical noise in dark-ground imaging

The preceding discussion focused on the photon shot-noise limit. As mentioned in section 3.2.2 for absorption imaging, it is very difficult to avoid technical noise such as spurious reflections and scattering by dust particles. Dark-ground imaging has the additional advantage of filtering out much of the technical noise. If, however, there is a remainder of this technical background present in the image, it will interfere with the signal of dark-ground imaging. Since the phase of the scattered background will be unknown and may vary spatially, this can cause considerable deterioration of the image.

5.3. Experimental dark-ground imaging

A striking example of the advantage of dark-ground imaging over absorption imaging can be seen in figure 6, demonstrating an increase in the SNR by almost one order of magnitude. Figure 6(a) shows an absorption image of 300–600 atoms with an SNR of about two. The atom clouds in the dark-ground images of figure 6(b) contain only about half as many atoms. The SNR however, is about five times better than that in absorption imaging. Both pictures were taken under the same imaging conditions. Despite figure 6(c) containing only 27 and 30 atoms, it achieves an SNR of 5, which is of the order of the atom-shot noise. This is especially impressive since the numerical aperture in the last image was limited to NA = 0.1, corresponding to a fluorescence collection efficiency of only 0.25%. It should also be noted that the imaging optics were constructed from standard off-the-shelf optics and had a working distance of 95 mm (see section A.1). It is worth noting that one can easily and reproducibly switch between dark-ground and absorption imaging simply by changing the angle of the probe beam and thus its position relative to the opaque disk.

In figure 7 we compare the atom numbers detected via dark-ground and absorption imaging in the diffraction-limited regime ($n\sigma = 0.2$ – 1.2), and find excellent agreement between the two methods. For each data point, we switched repeatedly between the two imaging techniques, taking a total of 250 pictures. Again, the only difference between the absorption and dark-ground images within one dataset was the angle of the probe beam.

As can be seen in figure 8, we also verified the dependence of the detected atom number in (9) on detuning (δ) and saturation (s_0). Figure 8(a) shows experimentally that the atom number calculated for dark-ground imaging according to (9) does not depend on the saturation parameter within a range of $s_0 = 0.05$ – 2 . Figure 8(b) depicts a frequency scan over the atomic line. For this we scanned the detection frequency over the resonance, taking a total of 117 images. We then fitted a Gaussian to each image and calculated the ‘atom number’ using (9) with the detuning set to zero ($\delta = 0$). Fitting a Lorentzian line-shape to the data, we find a

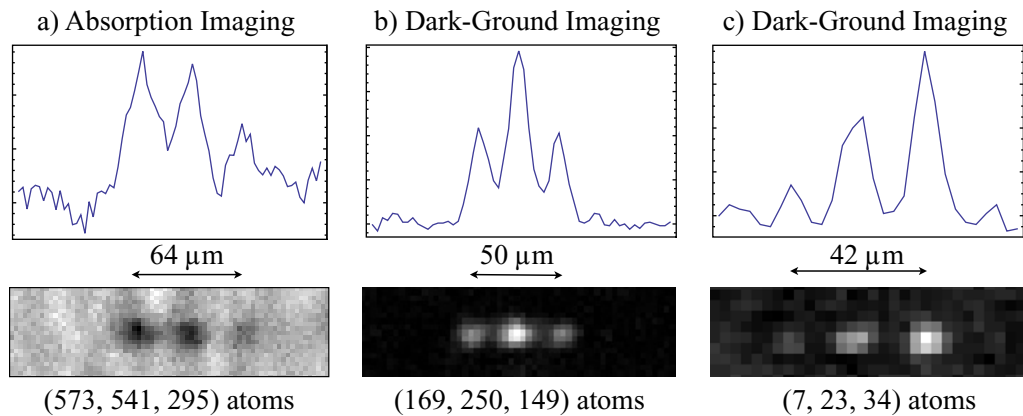


Figure 6. Images of spinor ^{87}Rb condensates after Stern–Gerlach separation. The exposure time was $200\ \mu\text{s}$ with π -polarized light at $s = 1$ on the $F = 2 \rightarrow 3$ transition of the D_2 line. (a) shows the transmittance T of an absorption image as described in section 3.1. The peak absorbance is about $A = 0.1$. (b) is the photon count in dark-ground images with a peak count of 200 photons per pixel corresponding to $A = 0.06$. (c) is the raw image of dark-ground imaging with a peak count of 60 photons per pixel corresponding to $A = 0.02$. The lowest atom number in the image corresponds to our detection limit of about seven atoms at an SNR of one. The only difference between the imaging conditions of (a) and (b) is the angle of the probe beam, which was changed by a few degrees for it to miss the dark spot and thus switch from dark-ground to absorption imaging. In all cases the dark spot had a diameter of $500\ \mu\text{m}$. Note that the dark-ground image contains far fewer atoms than the absorption image.

linewidth of 4.1 MHz, which is—due to saturation broadening—30% larger than the natural linewidth of the D_2 transition in rubidium.

It is interesting to note that the optical setup of this experiment can also be used for non-destructive imaging of dense atom clouds [16]. However, here we are concerned with low optical depths, where the contribution of the refractive dark-ground signal rapidly tends to zero because the refraction becomes too small to cause the light to be refracted around the dark spot. This can be seen in figure 8(b), where the signal strength fits nicely to the Lorentzian line shape predicted by (9). Complications due to refraction at higher optical depths can be avoided by resonant dark-ground imaging ($\delta = 0$).

6. Imaging errors

In both absorption and diffractive dark-ground imaging, it is important to understand how imperfections affect the shape of an image or the number of atoms detected. There are two different types of imaging errors: aberrations and diffraction. Aberrations distort the image: the shape of a small atom cloud might appear deformed or blurred, although generally no photons are lost. Diffraction causes part of the imaging information (photons) to be filtered out. The main effect of aberrations is to blur the image without losing photons. This does not affect fluorescence or absorption imaging at very low densities. At higher densities

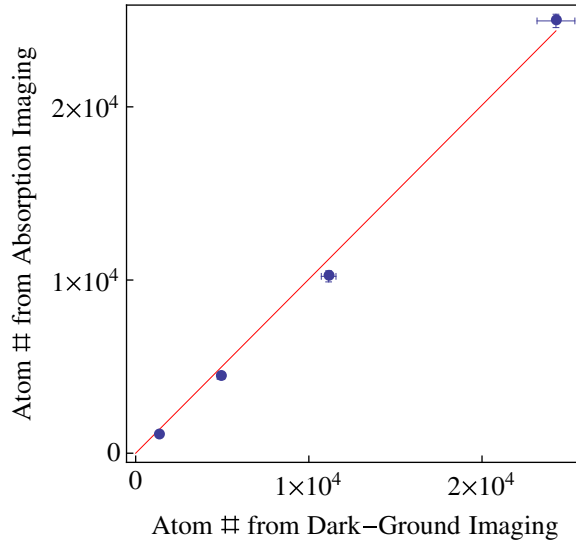


Figure 7. Direct comparison of the number of atoms detected with absorption and dark-ground imaging. Red — is the fit of a straight line to the data resulting in a slope of 1.0. The error bars are the standard error of the mean over 60 experimental realizations per point plotted. The main contribution to the error is probably a drift of the atom number when switching between the imaging techniques. The saturation parameter was on average $s_0 = 0.36$ and the detuning $\delta = 0$. The optical depth ($n\sigma$) ranged from 0.2 to 1.2, which means that the dark-ground imaging was performed in the diffraction-dominated regime.

and for dark-ground imaging though, the procedure for retrieval of atom column density from the images is nonlinear (see (3) and (9)). Any non-negligible aberration will result in an underestimation of the atom number. Since aberrations can be avoided by a high-quality objective and are difficult to treat generally, we will focus here on diffraction effects.

The diffracted image from a small atomic cloud evenly illuminates the objective lens. The observed image is therefore an Airy disc, which—when fitted with a Gaussian—gives the resolution limit of the objective as

$$w_{\min} = 0.595 \frac{\lambda}{\text{NA}}. \quad (11)$$

w_{\min} is the $1/e^2$ radius of a Gaussian fitted to the image of an object of negligible size. $\text{NA} = \rho/f$ is the numerical aperture of the objective and ρ is the radius of its limiting aperture. The solid green line in figure 9(a) shows this for our experimental conditions.

In order to investigate this effect more quantitatively, we have produced atom clouds close to the resolution limit of our imaging optics. We then artificially reduced the aperture of our imaging optics by placing an iris just after the second set of lenses. Figure 9(a) shows the $1/e^2$ radii of the fit of a Gaussian to the raw images as a function of numerical aperture. The solid green line shows the diffraction limit for a given numerical aperture according to (11). For small apertures, the images of the clouds are clearly diffraction limited. The e^{-2} radii of the fully resolved images are $\Delta x = 3.6 \mu\text{m}$ and $\Delta y = 5.2 \mu\text{m}$.

As mentioned earlier, the diffraction-limited image of an object is not ‘smudged’ by the limiting aperture but filtered. Figure 9(b) shows the loss in the integrated image intensity as

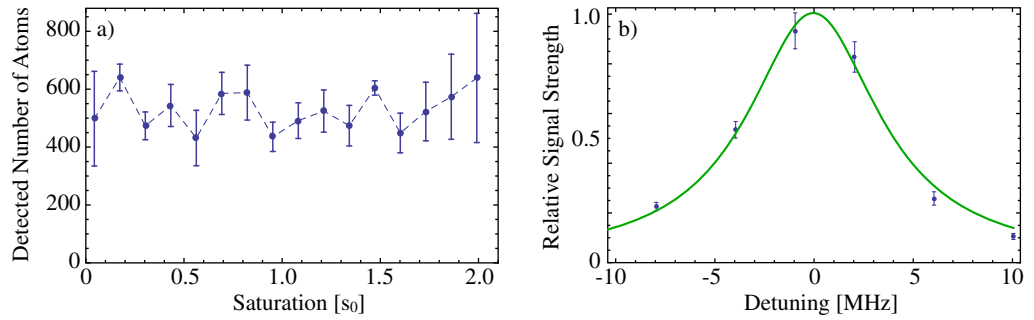


Figure 8. (a) Atom number in diffractive dark-ground imaging as a function of the saturation parameter from $s_0 = 0.05$ to $s_0 = 2$. The intensity of the probe beam was determined separately for each dark-ground image by multiplying the average intensity of the reference image by the measured extinction ratio of the dark spot ($I_{\text{ccd}}/I_0 = 9500$). The atom number was determined using (9). (b) Signal strength of diffractive dark-ground images versus detuning of the probe laser beam. The signal strength was determined using (9) with $\delta = 0$. Lime green — fit of a Lorentzian line to the data. The fitted half-width of 4.1 MHz is close to the saturation-broadened linewidth at $s_0 = 1$. The atom cloud contained about 7500 atoms with a resonant optical depth of $n\sigma_0 \simeq 2$. In both plots, the error bars correspond to the standard error of the mean of about 30 dark-ground images per plotted point.

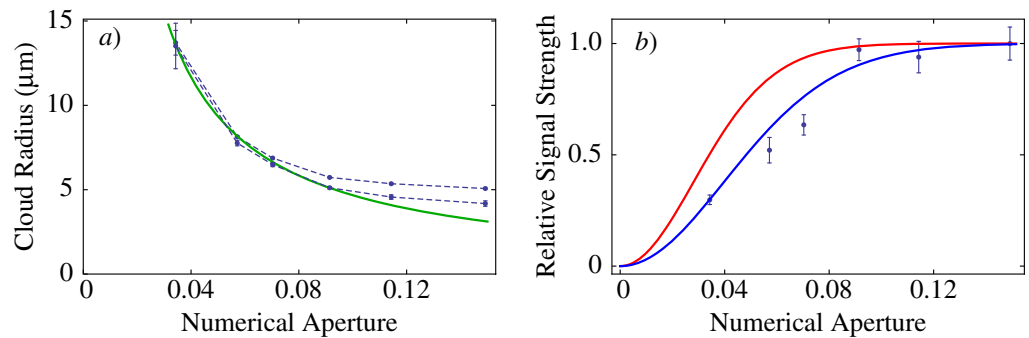


Figure 9. Effect of numerical aperture on dark imaging. (a) Size of the detected image as a function of numerical aperture. Lime green — diffraction limit according to (11). Blue ---- guide for the eye with the upper and lower lines standing for Δx and Δy , respectively. (b) Integrated intensity of the images as a function of numerical aperture. Blue — truncation of a Gaussian beam by the limiting aperture, calculated for a measured beam waist of $3.6 \mu\text{m} \times 5.2 \mu\text{m}$. Red — calculated truncation by the limited numerical aperture for a beam size of the calculated size of the atom cloud, which is $\sqrt{2}$ times larger than the beam waist for the blue line. The error bars are the standard error of the mean of about 30 realizations for each point.

a function of numerical aperture. We can calculate the expected reduction in integrated signal intensity by assuming that the images taken at large aperture represent a real object. We then propagate its shadow until the objective and integrate the transmitted intensity over the limiting

aperture. The blue line in figure 9(b) shows this for object sizes $\Delta x = 3.6 \mu\text{m}$ and $\Delta y = 5.2 \mu\text{m}$, which we determined from figure 9(a). The theory is clearly in good agreement with the data.

Figure 9, however, shows the sizes of the *images*, which are not necessarily equal to those of the atom clouds. For moderately low optical depths ($1 > n\sigma \gg 4\Omega$), the diffracted signal is proportional to the square of the optical depth (see the discussion below (8)). Therefore, a Gaussian-shaped cloud produces a Gaussian-shaped absorption shadow with a radius that is $\sqrt{2}$ smaller than the radius of the atom cloud. The red line in figure 9(b) shows the relative signal strength calculated without taking into account the increased diffraction for optically thin clouds. Clearly, the aperture of the imaging optics truncates the imaging beam much more than one would trivially expect from the size of the atomic cloud.

It should be noted that the reduction in the number of atoms detected can also lead to distortions of the cloud shape. Take the example of an elongated BEC that is well resolved in the axial direction and just below the resolution limit in the radial direction at the center of the BEC. Then the fraction of atoms detected will be larger in the center of the cloud as compared to the ends. This is because as one moves along the axis of the BEC the radial size of the BEC becomes smaller with the axial distance to the centre. Therefore, it becomes less resolved and a smaller fraction of the real atom number is detected. Since these arguments hold true for both absorption and dark-ground imaging, experimenters have to take great care when interpreting images of optically thin objects taken close to or below the diffraction limit of their optics. The resolution limit in this case is then $\Delta\rho_{\min} = 0.84 \frac{\lambda}{\text{NA}}$.

7. Optimal conditions for the imaging of small atom number clouds

7.1. Optimal detuning and saturation

We now consider optimal conditions for the imaging of atom clouds with low atom numbers, where the corresponding optical depths are small ($n\sigma_0 \ll 1$). Whereas [20] discusses minimally destructive imaging, here we are interested in measuring the shape of an atom cloud with the best SNR possible.

7.1.1. Absorption imaging. For small absorbances $A \simeq n\sigma' \ll 1$, we can rewrite (4b) as

$$\text{SNR}_{\text{abs}} = \frac{n(1 - \Omega)\sigma_0}{1 + s_0 + \delta^2} \sqrt{\frac{s_0 N_{\text{sat}}}{2}}, \quad (12)$$

where $N_{\text{sat}} \equiv N_0/s_0$ is the number of photo-electrons per pixel in the reference image at saturation intensity ($I_0 = I_{\text{sat}}$). Optimal detuning and saturation are therefore $\delta = 0$ and $s_0 = 1$, respectively. As mentioned earlier, numerical methods to model the reference image [22] can largely remove the photon shot-noise of the reference image, thus improving SNR_{abs} by a factor of $\sqrt{2}$.

Experimenters often use a weak probe beam in order to be able to neglect saturation effects. Using, for example, $s_0 = 0.1$ instead of the optimal $s_0 = 1$ reduces SNR by almost a factor of two.

7.1.2. Dark-ground imaging. For moderately low optical depths ($1 > n\sigma \gg \Omega$) the contribution from the dark-ground term $(n\sigma)^2$ dominates over that from the fluorescence term $(\Omega n\sigma)^2$

and we can rewrite (10) as

$$\text{SNR}_{\text{dark}} = \frac{n\sigma_0}{1 + s_0 + \delta^2} \sqrt{s_0 N_{\text{sat}}}, \quad (13)$$

which differs from SNR_{dark} in (12) only in that it is a factor of $\sqrt{2}$ larger. The optimal parameters for detuning and saturation are again $\delta = 0$ and $s_0 = 1$, respectively.

At even lower optical depths the contribution from fluorescence becomes more important, and for $n\sigma_0 \ll \Omega$ the term for fluorescence in (10) dominates the SNR. The SNR is then proportional to $\sqrt{s_0}$, and the image quality continues to increase with the saturation parameter until it becomes limited by the technical noise.

7.2. Optimal exposure time

Let us now optimize the detection for the lowest atom number in an atom cloud, which initially has a radius ρ . On the one hand, it is desirable to make the cloud as small as possible, because the SNRs in (12) and (13) are proportional to the column density. On the other hand, we would like to illuminate the atoms for as long as possible, because the SNRs are proportional to the square root of τ . Unfortunately, the scattered photons cause a random walk of the atoms in velocity space orthogonally to the imaging beam⁸, resulting in diffusion of the atoms by a distance

$$\Delta\rho = \frac{v_{\text{rec}}}{3} \left(\frac{2\Gamma s_0 \tau^3}{1 + s_0 + \delta^2} \right)^{1/2} \quad (14a)$$

$$= \frac{v_{\text{rec}}}{3} \sqrt{\Gamma \tau^3}, \quad \text{for } \delta = 0 \text{ and } s_0 = 1, \quad (14b)$$

where Γ is the upper state decay rate and $v_{\text{rec}} = \hbar k/m$ is the recoil velocity.

A cloud with a radius ρ_0 before the imaging will therefore have a size of $\rho' = \sqrt{\Delta\rho^2 + \rho_0^2}$ after interaction with the probe beam. Using this size in order to calculate the SNR in (12) or (13) and then optimizing the exposure time, we find that the optimum exposure time for both dark-ground and absorption imaging is

$$\tau_{\text{opt}} = \left(\frac{9\rho_0^2}{2v_{\text{rec}}^2 \Gamma} \right)^{1/3}. \quad (15)$$

A more thorough analysis requires one to calculate the average of the signal over the expansion time rather than its final size only. In absorption imaging, one then finds a slightly longer optimal expansion time of $\tau'_{\text{opt}} = 1.46\tau_{\text{opt}}$, resulting in an increase in the fitted cloud size by 11% during the imaging process. For an exposure time of τ_{opt} , the fitted cloud size increases by only 5%. One also finds that even if the initial and final clouds are of Gaussian shape, the final image will not be Gaussian, since the image is the result of the sum over Gaussians of increasing size. Similar arguments apply to the inverted parabola of condensates. In absorption imaging, the exposure time does not affect the atom number as detected by integrating the signal. A Gaussian fit will underestimate the atom number by 0.5% at τ_{opt} , by 3% at τ'_{opt} , and by 8% at $2\tau_{\text{opt}}$.

⁸ The acceleration of atoms toward the camera due to light pressure can usually be neglected due to the Rayleigh range of imaging optics being much larger than the resolution.

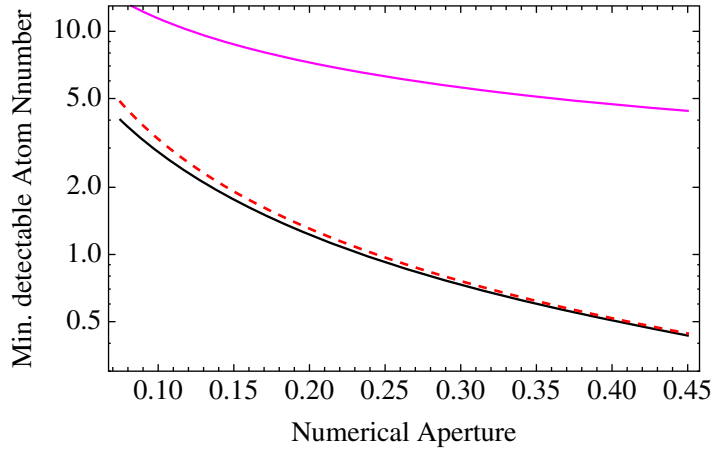


Figure 10. Plot of the minimum detectable atom number in an ^{87}Rb atom cloud with $\text{SNR} = 1$ at the central pixel assuming optimal imaging parameters using (15), $\delta = 0$ and $s = 1$: Rhodamine — absorption, red - - - fluorescence and black — dark-ground imaging.

In dark-ground imaging, the photon shot-noise-limited SNR continues to increase with the exposure time but saturates quickly after a few τ_{opt} . At $\tau = \tau_{\text{opt}}$, the SNR reaches 81% of its maximum. The fitted cloud size increases by only 5% and the atom number calculated by a Gaussian fit using (9) stays accurate to within 1%. At $\tau = \tau'_{\text{opt}}$, the SNR reaches 93% of its maximum value, the apparent cloud size increases by only 9%, and the atom number calculated from a Gaussian fit using (9) stays accurate to within 5%.

7.3. Optimal size of the dark spot and probe beam

As pointed out in section 5, the dark spot has to be much larger than the focal spot of the probe beam, but much smaller than the collimated diffraction from the atom cloud. The size of the dark spot therefore imposes a lower limit on the size of the probe beam and an upper limit on the size of the atom cloud:

$$w_0 \ll \frac{f\lambda}{\pi w_{\text{dark}}} \ll w_{\text{probe}}, \quad (16)$$

where w_{probe} is the $1/e^2$ radius of the probe beam and w_0 is the $1/e^2$ radius of the image of the cloud. Since in practice one is usually limited by optical fringes and scattered light, it is advantageous to use a small w_{probe} and to choose a much larger w_{dark} than suggested by the right side of the inequality. Inserting our standard conditions ($\lambda = 780 \text{ nm}$, $f = 95 \text{ mm}$, $w_{\text{dark}} = 200 \mu\text{m}$ and $w_{\text{probe}} = 1 \text{ mm}$) into (16), we find for the cloud size $w_0 \ll 120 \mu\text{m} \ll 1 \text{ mm}$.

7.4. Optimal cloud size

If we input the optimal expansion time, saturation parameter and detuning into (12) or (13), we find $\text{SNR}_{\text{opt}} \propto \rho_0^{-2/3}$. Both for absorption imaging and in the diffraction-dominated regime of dark-ground imaging, it is therefore desirable to make the atom cloud as small as possible. However, as seen in section 6, care has to be taken to stay well within the resolution limit of the imaging optics.

7.5. Minimum detectable atom number

Assuming that the atom cloud is slightly ($2\times$) larger than the optical resolution⁹, we can calculate the optimum exposure time $1.5\tau_{\text{opt}}$ for absorption and dark-ground imaging from (15). We set the pixel size equal to the optical resolution. We insert these conditions into the SNR for the central pixel in absorption imaging (4a) and dark-ground imaging (10). Figure 10 shows the result of setting $\text{SNR} = 1$ for the central pixel and solving numerically for the atom number. In interpreting the results, care has to be taken because the validity of the equations for the absorption and dark-ground images relies on the coherent addition of the contribution of many atoms, whereas the description of fluorescence contribution is valid down to a single atom. For the parameter regime chosen here, the dark-ground signal is dominated by the contribution from the fluorescence and reaches the single-atom limit at about $\text{NA} = 0.45$. Note that over the whole range dark-ground imaging (black) can detect far fewer atoms than absorption imaging (magenta).

8. Conclusions

In this paper, we demonstrated and analyzed a novel imaging technique—diffractive dark-ground imaging—and showed experimentally that using very moderate detection optics ($\text{NA} = 0.1$) it can detect down to a few tens of atoms with near-atom shot-noise-limited precision. Using high-NA optics, *in situ* dark-ground imaging will be possible for the first time with single-atom resolution.

We also analyzed absorption imaging and presented for the first time an analytic expression for the atom column density from absorption images, including saturation and fluorescence effects. We pointed out some potentially serious imaging errors and how to avoid them.

Acknowledgments

We thank Giorgos Konstantinidis for supplying early versions of the dark spot. We also thank the anonymous referees for critical comments. This work was supported by a Marie Curie Excellence Grant of the European Communities Sixth Framework Programme under Contract MEXT-CT-2005-024854 and by FONCICyT project number 94142. PCC and DS acknowledge the National Research Foundation and the Ministry of Education, Singapore.

Appendix A. Experimental setup

A.1. Imaging optics

We use a relay telescope that consists of two identical sets of off-the-shelf achromatic lenses (see figures 1 and 5) followed by a microscope objective and the CCD camera. Each of the two sets of lenses consists of an achromatic doublet (Melles-Griot, LAO-160.0-31.5-780, effective diameter 28.35 mm, focal length $f = 160.0$ mm) and a companion meniscus lens (Melles-Griot, MENP-31.5-6.0-233.6-780, $f = 233.6$ mm)¹⁰. We place the meniscus 1 mm after the

⁹ Note that as the atom number approaches unity the diffraction part of (7) is strongly reduced, since the size of a single atom is not well defined. However, for clouds of a few atoms this contribution is already negligible.

¹⁰ The part-numbers and trade names used in this paper are for identification purposes only and do not constitute an endorsement by the authors or their institutions.

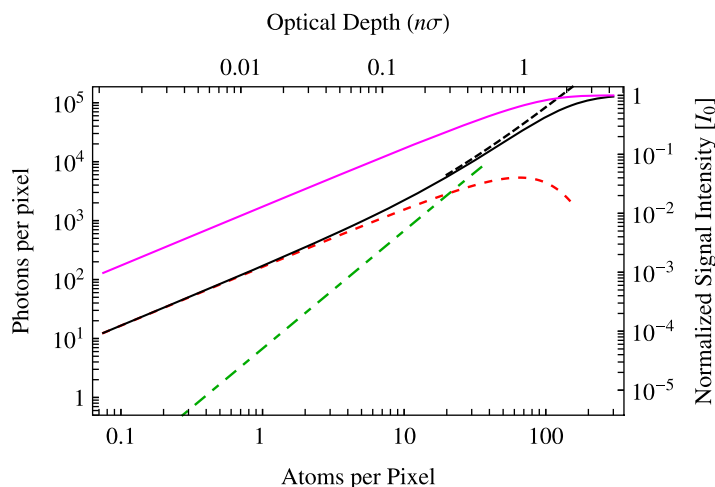


Figure B.1. Signal strength in imaging: a plot of the signal intensity of the absorption, fluorescence and dark-ground images versus atom column densities. The left and lower axes stand for the number of photons and atoms per pixel, respectively, using the experimental parameters described below. The upper axis is the optical depth in units of $n\sigma$, and the right axis is the image intensity relative to the intensity of the probe beam, here $I_0 = I_{\text{sat}}$. Rhodamine — signal in absorption imaging [$I_0(1 - T)$] using (2). Black — full dark-ground signal from (7). Black - - - approximation of the dark-ground signal for low absorbances ($n\sigma \ll 1$) according to (8). Red - - - contribution of the fluorescence to the dark-ground signal. Lime green — · — contribution to the dark-ground signal by the light that was diffracted by the atom cloud. The parameters are the same as in figure 2, except for the numerical aperture and thus collection efficiency, which are here $\text{NA} = 0.59$ and $\Omega = 0.09$, respectively. The pixel size is $1 \mu\text{m}$.

doublet, thus reducing the total focal length to 95.5 mm. For magnification, we use DIN Microscope Objectives (Edmund Optics) that provide us with magnifications $M = 10$ (NT43-907) and $M = 4$ (NT38-341). The effective numerical apertures are $\text{NA} = 0.15$ and $\text{NA} = 0.08$, respectively. The collection efficiencies are $\Omega = 0.5\%$ and $\Omega = 0.25\%$. In some of the images, 2×2 binning in the camera was employed, resulting in an effective magnification of $5\times$ and an effective pixel size of $2.6 \mu\text{m}$.

For dark-ground imaging, a dark spot (Melles-Griot) is placed between the two sets of lenses in the relay objective. The mask consists of an antireflection-coated window of diameter 30 mm and thickness 2 mm with an opaque disc in its center. The disc is made of chrome-LRC and has optical density $\text{OD} > 4$ and reflectivity $R < 15\%$ at 780 nm. The diameters of the dots on the mask range from $20 \mu\text{m}$ to 5 mm. In order to minimize scattering and interference, the diameter of the probe beam was kept as small as possible, typically 2 mm. Note that one can change between dark-ground and absorption imaging simply by changing the angle of the imaging beam and thus whether or not it is blocked by the dark-ground mask.

Our camera is the Andor iKon-M (DU934N-BR-DD) low-noise CCD camera. The pixel size is $13.3 \mu\text{m} \times 13.3 \mu\text{m}$ image area. The well depth is 100 000 electrons with a dynamic range of 65 535. The quoted quantum efficiency is 95% at 780 nm.

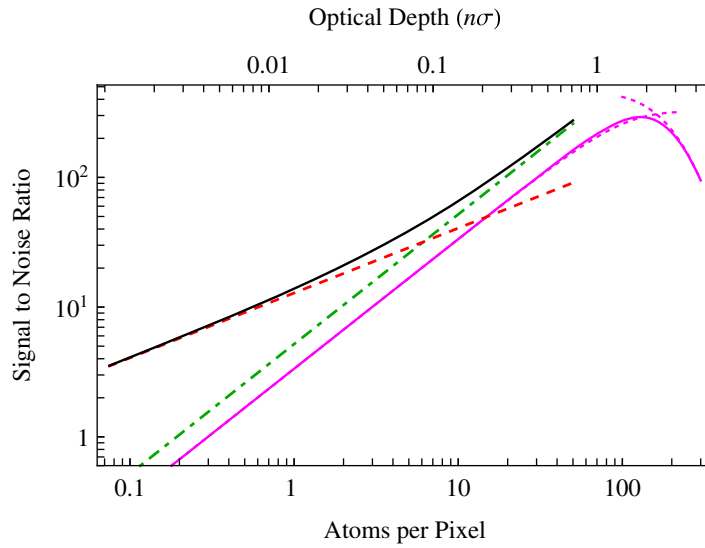


Figure B.2. Photon shot-noise limited SNR: a plot of the photon shot-noise-limited SNR versus the optical depth for dark-ground, fluorescence and absorption imaging of an atom cloud. The lower axis represents the number of atoms per pixel and the upper axis is the unsaturated resonant optical depth $n\sigma_0$. Rhodamine — SNR of absorption imaging according to (4a). Rhodamine $\cdots\cdots$ approximations of the SNR of absorption imaging for $n\sigma \ll 1$ and $T \ll 1$, respectively, according to (4b). Black — SNR of dark imaging for low absorbances according to (10). Red - - - SNR of the fluorescence alone. Lime green — · — SNR of the light that was diffracted by the atom cloud. The parameters are the same as in figure B.1. They are the same as in figure 3, except for the numerical aperture and thus collection efficiency, which are here $NA = 0.59$ and $\Omega = 0.09$, respectively. The pixel size is $1 \mu\text{m}$.

We image on the $F = 2 \rightarrow F = 3$ transition of the D_2 line in ^{87}Rb at 780 nm. The images presented in the paper were taken with an expansion time of 1.5–2.5 ms and exposure times of 100–200 μs .

A.2. Low atom number generation

To reach the desired atom number, we load for 7–20 s an atom flux of $2 \times 10^8 \text{ atom s}^{-1}$ from a 2D-MOT into the 3D-MOT ($B'_\rho = 4 \text{ G cm}^{-1}$). After compression, optical molasses, and transfer to the TOP trap ($B'_\rho = 56 \text{ G cm}^{-1}$, $B_{\text{TOP}} = 40 \text{ G}$) we find about 2×10^9 atoms in the $|F = 2, m_F = 2\rangle$ state at a temperature of about 100 μK . The quadrupole field is then ramped up to 216 G cm^{-1} in 15 s. We then ramp in 25 s the TOP field down to $B_{\text{TOP}} = 4 \text{ G}$. Finally, we ramp in 4 s the TOP field down to $B_{\text{TOP}} = 70\text{--}100 \mu\text{G}$, resulting in trapping frequencies of up to $\omega_\rho/2\pi = 700 \text{ Hz}$ and $\omega_z/2\pi = 2 \text{ kHz}$. This procedure reliably produces BECs of tens to hundreds of atoms even without using RF-induced forced evaporation. If we wish larger BECs we choose larger TOP field amplitudes and evaporate the atoms using an RF-field that is ramped from 50 to 2.2 MHz in 25 s. During the switching-off of the quadrupole field, we can apply a rapid sweep of the magnetic field, which for very low B_{TOP} partially depolarizes the sample.

The distribution among the m_F states can be adjusted by changing the duration and magnitude of the sweep.

Appendix B. Additional graphs

B.1. Large NA optics

Here, we re-plot figures 2 and 3 for the objective used in [4], which has a diffraction-limited numerical aperture of $NA = 0.59$ and a collection efficiency of $\Omega = 0.09$, resulting in a resolution of $1.1 \mu\text{m}$ at 780 nm (figures B.1 and B.2). The pixel size is set at $1 \mu\text{m}$. The minimum detectable optical depth improves by a factor of ten as compared to our previous experimental parameters (see figure 3). Single-atom detection should be possible with this objective.

References

- [1] Bradley C C, Sackett C A, Tollett J J and Hulet R G 1995 *Phys. Rev. Lett.* **75** 1687–90
- [2] Davis K, Mewes M, Andrews M, van Druten N, Durfee D, Kurn D and Ketterle W 1995 *Phys. Rev. Lett.* **75** 3969–73
- [3] Anderson M H, Ensher J R, Matthews M R, Wieman C E and Cornell E A 1995 *Science* **269** 198–201
- [4] Estève J, Gross C, Weller A, Giovanazzi S and Oberthaler M 2008 *Nature* **455** 1216–9
- [5] Gerbier F, Fölling S, Widera A, Mandel O and Bloch I 2006 *Phys. Rev. Lett.* **96** 90401
- [6] Fölling S, Gerbier F, Widera A, Mandel O, Gericke T and Bloch I 2005 *Nature* **434** 481–4
- [7] Bouyer P and Kasevich M A 1997 *Phys. Rev. A* **56** R1083–6
- [8] Bloch I, Dalibard J and Zwierger W 2008 *Rev. Mod. Phys.* **80** 885–964
- [9] Hu Z and Kimble H 1994 *Opt. Lett.* **19** 1888–90
- [10] Frese D, Ueberholz B, Kuhr S, Alt W, Schrader D, Gomer V and Meschede D 2000 *Phys. Rev. Lett.* **85** 3777–80
- [11] Bakr W S, Gillen J I, Peng A, Fölling S and Greiner M 2009 *Nature* **462** 74–7
- [12] Weitenberg C, Endres M, Sherson J F, Cheneau M, Schausz P, Fukuhara T, Bloch I and Kuhr S 2011 *Nature* **471** 319–24
- [13] Schellekens M, Hoppeler R, Perrin A, Gomes J V, Boiron D, Aspect A and Westbrook C I 2005 *Science* **310** 648–51
- [14] Bücke R, Perrin A, Manz S, Betz T, Koller C, Plisson T, Rottmann J, Schumm T and Schmiedmayer J 2009 *New J. Phys.* **11**
- [15] Ketterle W, Durfee D and Stamper-Kurn D 1999 *Bose–Einstein Condensation in Atomic Gases, Proc. Int. School of Physics ‘Enrico Fermi’* vol CXL, ed M Inguscio, S Stringari and C Wieman (Amsterdam: IOS Press) pp 67–176
- [16] Andrews M R, Mewes M O, van Druten N J, Durfee D S, Kurn D M and Ketterle W 1996 *Science* **273** 84–7
- [17] Andrews M R, Kurn D M, Miesner H J, Durfee D S, Townsend C G, Inouye S and Ketterle W 1997 *Phys. Rev. Lett.* **79** 553–6
- [18] Turner L D, Domen K F E M and Scholten R E 2005 *Phys. Rev. A* **72** 031403
- [19] Kadlecik S, Sebby J, Newell R and Walker T G 2001 *Opt. Lett.* **26** 137–9
- [20] Hope J J and Close J D 2004 *Phys. Rev. Lett.* **93** 180402
- [21] Reinaudi G, Lahaye T, Wang Z and Guéry-Odelin D 2007 *Opt. Lett.* **32** 3143–5
- [22] Ockeloen C F, Tauschinsky A F, Spreeuw R J C and Whitlock S 2010 *Phys. Rev. A* **82** 061606